



HAL
open science

Euclid preparation. XVII. Cosmic Dawn Survey: Spitzer Space Telescope observations of the Euclid deep fields and calibration fields

A. Moneti, H. J. Mccracken, M. Shuntov, O. B. Kauffmann, P. Capak, I. Davidzon, O. Ilbert, C. Scarlata, S. Toft, J. Weaver, et al.

► To cite this version:

A. Moneti, H. J. Mccracken, M. Shuntov, O. B. Kauffmann, P. Capak, et al.. Euclid preparation. XVII. Cosmic Dawn Survey: Spitzer Space Telescope observations of the Euclid deep fields and calibration fields: XVII. Cosmic Dawn Survey: Spitzer Space Telescope observations of the Euclid deep fields and calibration fields. *Astronomy and Astrophysics - A&A*, 2022, 658, pp.A126. 10.1051/0004-6361/202142361 . hal-03565435

HAL Id: hal-03565435

<https://hal.science/hal-03565435>

Submitted on 10 Feb 2022

HAL is a multi-disciplinary open access archive for the deposit and dissemination of scientific research documents, whether they are published or not. The documents may come from teaching and research institutions in France or abroad, or from public or private research centers.

L'archive ouverte pluridisciplinaire **HAL**, est destinée au dépôt et à la diffusion de documents scientifiques de niveau recherche, publiés ou non, émanant des établissements d'enseignement et de recherche français ou étrangers, des laboratoires publics ou privés.

Euclid preparation

XVII. Cosmic Dawn Survey: *Spitzer* Space Telescope observations of the *Euclid* deep fields and calibration fields

Euclid Collaboration: A. Moneti¹, H. J. McCracken^{1,2}, M. Shuntov¹, O. B. Kauffmann³, P. Capak⁴, I. Davidzon⁴, O. Ilbert³, C. Scarlata⁵, S. Toft^{6,7}, J. Weaver⁴, R. Chary⁸, J. Cuby³, A.L. Faisst⁹, D. C. Masters⁹, C. McPartland^{4,10,11}, B. Mobasher¹⁰, D. B. Sanders¹¹, R. Scaramella^{12,13}, D. Stern¹⁴, I. Szapudi¹¹, H. Teplitz⁸, L. Zalesky¹¹, A. Amara¹⁵, N. Auricchio¹⁶, C. Bodendorf¹⁷, D. Bonino¹⁸, E. Branchini^{19,20}, S. Brau-Nogue²¹, M. Brescia²², J. Brinchmann^{23,24}, V. Capobianco¹⁸, C. Carbone²⁵, J. Carretero^{26,27}, F. J. Castander^{28,29}, M. Castellano¹³, S. Cavuoti^{22,30,31}, A. Cimatti^{32,33}, R. Cledassou^{34,35}, G. Congedo³⁶, C. J. Conselice³⁷, L. Conversi^{38,39}, Y. Copin⁴⁰, L. Corcione¹⁸, A. Costille³, M. Cropper⁴¹, A. Da Silva^{42,43}, H. Degaudenzi⁴⁴, M. Douspis⁴⁵, F. Dubath⁴⁴, C. A. J. Duncan⁴⁶, X. Dupac³⁹, S. Dusini⁴⁷, S. Farrens⁴⁸, S. Ferriol⁴⁰, P. Fosalba^{28,29}, M. Frailis⁴⁹, E. Franceschi¹⁶, M. Fumana²⁵, B. Garilli²⁵, B. Gillis³⁶, C. Giocoli^{50,51}, B. R. Granett⁵², A. Grazian⁵³, F. Grupp^{17,54}, S. V. H. Haugan⁵⁵, H. Hoekstra⁵⁶, W. Holmes¹⁴, F. Hormuth^{57,58}, P. Hudelot¹, K. Jahnke⁵⁸, S. Kermiche⁵⁹, A. Kiessling¹⁴, M. Kilbinger⁴⁸, T. Kitching⁴¹, R. Kohley³⁹, M. Kümmel⁵⁴, M. Kunz⁶⁰, H. Kurki-Suonio⁶¹, S. Ligori¹⁸, P. B. Lilje⁵⁵, I. Lloro⁶², E. Maiorano¹⁶, O. Mansutti⁴⁹, O. Marggraf⁶³, K. Markovic¹⁴, F. Marulli^{16,64,65}, R. Massey⁶⁶, S. Maurogordato⁶⁷, M. Meneghetti^{9,16,65}, E. Merlin¹³, G. Meylan⁶⁸, M. Moresco^{16,64}, L. Moscardini^{16,64,65}, E. Munari⁴⁹, S. M. Niemi⁶⁹, C. Padilla²⁷, S. Paltani⁴⁴, F. Pasian⁴⁹, K. Pedersen⁷⁰, S. Pires⁴⁸, M. Poncet³⁵, L. Popa⁷¹, L. Pozzetti¹⁶, F. Raison¹⁷, R. Rebolo^{72,73}, J. Rhodes¹⁴, H. Rix⁵⁸, M. Roncarelli^{16,64}, E. Rossetti⁶⁴, R. Saglia^{17,54}, P. Schneider⁶³, A. Secroun⁵⁹, G. Seidel⁵⁸, S. Serrano^{28,29}, C. Sirignano^{47,74}, G. Sirri⁶⁵, L. Stanco⁴⁷, P. Tallada-Crespí^{26,75}, A. N. Taylor³⁶, I. Tereno^{42,76}, R. Toledo-Moreo⁷⁷, F. Torradeflot^{26,75}, Y. Wang⁸, N. Welikala³⁶, J. Weller^{17,54}, G. Zamorani¹⁶, J. Zoubian⁵⁹, S. Andreon⁵², S. Bardelli¹⁶, S. Camera^{18,78,79}, J. Graciá-Carpio¹⁷, E. Medinaceli⁵⁰, S. Mei⁸⁰, G. Polenta⁸¹, E. Romelli⁴⁹, F. Sureau⁴⁸, M. Tenti⁶⁵, T. Vassallo⁵⁴, A. Zacchei⁴⁹, E. Zucca¹⁶, C. Baccigalupi^{49,82,83,84}, A. Balaguera-Antolínez^{72,73}, F. Bernardeau⁸⁵, A. Biviano^{49,82}, M. Bolzonella¹⁶, E. Bozzo⁴⁴, C. Burigana^{86,87,88}, R. Cabanac²¹, A. Cappi^{16,67}, C. S. Carvalho⁷⁶, S. Casas⁴⁸, G. Castignani^{16,64}, C. Colodro-Conde⁷³, J. Coupon⁴⁴, H. M. Courtois⁸⁹, D. Di Ferdinando⁶⁵, M. Farina⁹⁰, F. Finelli^{86,91}, P. Flose-Reimberg¹, S. Fotopoulou⁹², S. Galeotta⁴⁹, K. Ganga⁸⁰, J. Garcia-Bellido⁹³, E. Gaztanaga^{28,29}, G. Gozaliasi^{94,95}, I. Hook⁹⁶, B. Joachimi⁹⁷, V. Kansal⁴⁸, E. Keihanen⁹⁵, C. C. Kirkpatrick⁶¹, V. Lindholm^{95,98}, G. Mainetti⁹⁹, D. Maino^{25,100,101}, R. Maoli^{13,102}, M. Martinelli⁹³, N. Martinet³, M. Maturi^{103,104}, R. B. Metcalfe^{64,91}, G. Morgante¹⁶, N. Morisset⁴⁴, A. Nucita^{105,106}, L. Patrizii⁶⁵, D. Potter¹⁰⁷, A. Renzi^{47,74}, G. Riccio²², A. G. Sánchez¹⁷, D. Sapone¹⁰⁸, M. Schirmer⁵⁸, M. Schultheis⁶⁷, V. Scottez¹, E. Sefusatti^{49,82,84}, R. Teyssier¹⁰⁷, O. Tubio⁷³, I. Tutusaus^{28,29}, J. Valiviita^{98,109}, M. Viel^{49,82,83,84}, and H. Hildebrandt¹¹⁰

(Affiliations can be found after the references)

Received 4 October 2021 / Accepted 21 November 2021

ABSTRACT

We present a new infrared survey covering the three *Euclid* deep fields and four other *Euclid* calibration fields using *Spitzer* Space Telescope's Infrared Array Camera (IRAC). We combined these new observations with all relevant IRAC archival data of these fields in order to produce the deepest possible mosaics of these regions. In total, these observations represent nearly 11 % of the total *Spitzer* Space Telescope mission time. The resulting mosaics cover a total of approximately 71.5 deg² in the 3.6 and 4.5 μm bands, and approximately 21.8 deg² in the 5.8 and 8 μm bands. They reach at least 24 AB magnitude (measured to 5σ, in a 2''5 aperture) in the 3.6 μm band and up to ~5 mag deeper in the deepest regions. The astrometry is tied to the *Gaia* astrometric reference system, and the typical astrometric uncertainty for sources with 16 < [3.6] < 19 is ≤ 0''.15. The photometric calibration is in excellent agreement with previous WISE measurements. We extracted source number counts from the 3.6 μm band mosaics, and they are in excellent agreement with previous measurements. Given that the *Spitzer* Space Telescope has now been decommissioned, these mosaics are likely to be the definitive reduction of these IRAC data. This survey therefore represents an essential first step in assembling multi-wavelength data on the *Euclid* deep fields, which are set to become some of the premier fields for extragalactic astronomy in the 2020s.

Key words. cosmology: observations – large-scale structure of Universe – dark energy – dark matter – Galaxy: formation – surveys

1. Introduction

The *Euclid* mission will survey 15 000 deg² of the extragalactic sky to investigate the nature of dark energy and dark matter and to study the formation and evolution of galaxies (Laureijs et al. 2011). To this end, *Euclid* will obtain high resolution and high signal-to-noise imaging of a billion galaxies in a broad optical filter to measure their shapes, and in three near-infrared (NIR) filters to measure their colours. It will also obtain high signal-to-noise NIR spectroscopy of about thirty million of these galaxies to measure abundances and redshifts. Additionally, photometric redshifts will be determined by combining the *Euclid* data with optical photometry from external surveys.

To reach the required precision on cosmological parameters and satisfy the stringent mission requirements on completeness and spectroscopic purity and to shape noise bias, *Euclid* must also obtain observations with a 40 times longer exposure per pixel than the main survey over regions covering at least 40 deg². To this end, three ‘deep’ fields were selected by the *Euclid* Consortium. They are described in detail in Scaramella et al. (in prep.), which gives references to prior studies; we give just a very brief description here. They are as follows: (1) *Euclid* Deep Field North (EDF-N), a roughly circular, 10 deg² region centred on the well-studied north Ecliptic pole; (2) *Euclid* Deep Field Fornax (EDF-F), also roughly circular and of 10 deg², centred on the *Chandra* Deep Field South (CDF-S, Mauduit et al. 2012; Lacy et al. 2021), and including the GOODS-S (Giavalisco et al. 2004) and the *Hubble* Ultra Deep Field (HUDF, Beckwith et al. 2006); and (3) the *Euclid* Deep Field South (EDF-S), a pill-shaped area of 20 deg² with no previous dedicated observations. In addition to these three deep fields, *Euclid* will observe several fields for the calibration of photometric redshifts (photo-*z*). These fields need to be observed to a level five times deeper than the main survey, and they are centred on some of the best studied extragalactic survey fields that already have extensive spectroscopic data: (1) the COSMOS field (Scoville et al. 2007; Sanders et al. 2007), (2) the Extended Groth Strip (EGS, Grogin et al. 2011), (3) the *Hubble* Deep Field North (HDF, also GOODS-N), and (4) the XMM-Large Scale Structure Survey field, which includes the Subaru XMM Deep Survey field (SXDS, Lonsdale et al. 2003; Mauduit et al. 2012; Lacy et al. 2021), and the VIMOS VLT Deep Survey (VVDS)¹.

While *Euclid* will observe these fields primarily for calibration purposes, those observations will provide an unprecedented data set to study galaxies at faint magnitudes and high redshifts. The survey efficiency of *Euclid* in the NIR bands is orders of magnitude greater than that of ground-based telescopes (e.g. VISTA). The *Euclid* deep fields alone will be 30 times larger and one magnitude deeper than the latest UltraVISTA data release (Moneti et al. 2019) covering the COSMOS field and will reach a depth of 26 mag in the *Y*, *J*, and *H* filters (5σ). In addition, *Euclid* carries a wide-field near-infrared grism spectrograph, the Near Infrared Spectrometer and Photometer (NISF), covering the $0.92 < \lambda < 1.85 \mu\text{m}$ region, which will provide multiple spectra at numerous grism orientations for more than one million sources to a line flux limit similar to 3D-HST (Brammer et al. 2012) and over an area 200 times larger than the COSMOS field (depending on the scheduling of the blue grism observations). The observations of the deep fields will result in the most complete and deepest spectroscopic coverage produced by *Euclid*. Such a spectroscopic data set will be unique for the reconstruc-

tion of the galaxy environment at cosmic noon and for measuring the star formation rate from the H α emission line intensity.

The deep and wide NIR data from *Euclid* are also ideal for detecting significant numbers of high-redshift ($7 < z < 10$) galaxies, as the Lyman α line is redshifted out of the optical into the NIR. However, in order to distinguish galaxy candidates from stars (primarily brown dwarfs), faint Balmer-break galaxies, and dusty star-forming galaxies at lower redshifts, which can all have similar NIR magnitudes and colours, deep optical, and mid-infrared (MIR) data are also needed (Bouwens et al. 2019; Bridge et al. 2019; Bowler et al. 2020).

The Cosmic Dawn Survey (Toft et al., in prep.) aims to obtain uniform, multi-wavelength imaging of the *Euclid* deep and calibration fields to limits matching the *Euclid* data for the characterisation of high-redshift galaxies. The optical data will be provided by the Hawaii-Two-0 Subaru telescope/Hyper-SuprimeCam (HSC) survey (McPartland et al., in prep.) for the EDF-N and EDF-F, and likely by the *Vera C. Rubin* Observatory for EDF-S and EDF-F. For the COSMOS and SXDS fields, optical data are provided by the Subaru HSC Strategic programme (HSC-SSP, Aihara et al. 2011).

In this paper, we present the *Spitzer* Space Telescope (Werner et al. 2004) component of the Cosmic Dawn Survey, which consists of (1) observing the full extent of the deep fields at 3.6 and 4.5 μm (only small parts of the EDF-N and EDF-F had already been observed with IRAC, see above), and (2) processing the new observations together with all relevant archival IRAC data, thus including data at 5.8 and 8.0 μm obtained during the cryogenic mission, and tying them to the latest *Gaia* astrometric reference system. In this way, we strive to produce the deepest possible and most modern MIR images (mosaics) of the deep and calibration fields.

In addition to being essential for the identification of high-redshift galaxies, MIR data are crucial for revealing the stellar mass content of the high-redshift Universe (which is outside the scope of *Euclid* core science). The *Euclid* data alone are not sufficient to characterise the stellar masses at $z > 3.5$, as the Balmer break is redshifted out of the reddest band of the NISP. Without MIR data, the interpretation of spectral energy distributions (SEDs) would rely on rest-frame ultraviolet emission which is strongly affected by dust attenuation and dominated by stellar light of new-born stars. Therefore, integrated quantities like the stellar mass would be highly unreliable (Bell & de Jong 2001). Moreover, photometric redshifts would be prone to catastrophic failures resulting from the misidentification of the Lyman and Balmer breaks (e.g. Le Fèvre et al. 2015; Kauffmann et al. 2020). In summary, *Spitzer* Space Telescope/IRAC data are crucial for identifying the most distant objects (e.g. Bridge et al. 2019), for improving the accuracy of their photometric redshifts, and deriving their physical properties such as stellar masses, dust content, age, and star-formation rate from population synthesis models (e.g. Pérez-González et al. 2008; Caputi et al. 2015; Davidzon et al. 2017). The build-up of stellar mass, especially when confronted with the amount of matter residing in dark matter halos at high redshifts can be a highly discriminating test for galaxy formation models (Legrand et al. 2019). The extrapolation of recent work in the COSMOS field (Bowler et al. 2020) suggests that hundreds of the rarest, brightest $z > 7$ galaxies are expected to be discovered in the *Euclid* deep fields. These provide unique constraints on cosmic reionisation, as the brightest galaxies form in the highest density regions of the Universe, which are expected to be the sites of the first generation of stars and galaxies, and thus of reionisation bubbles (Trac et al. 2008).

¹ These are now known as the “*Euclid* Auxiliary Fields” in *Euclid* terminology.

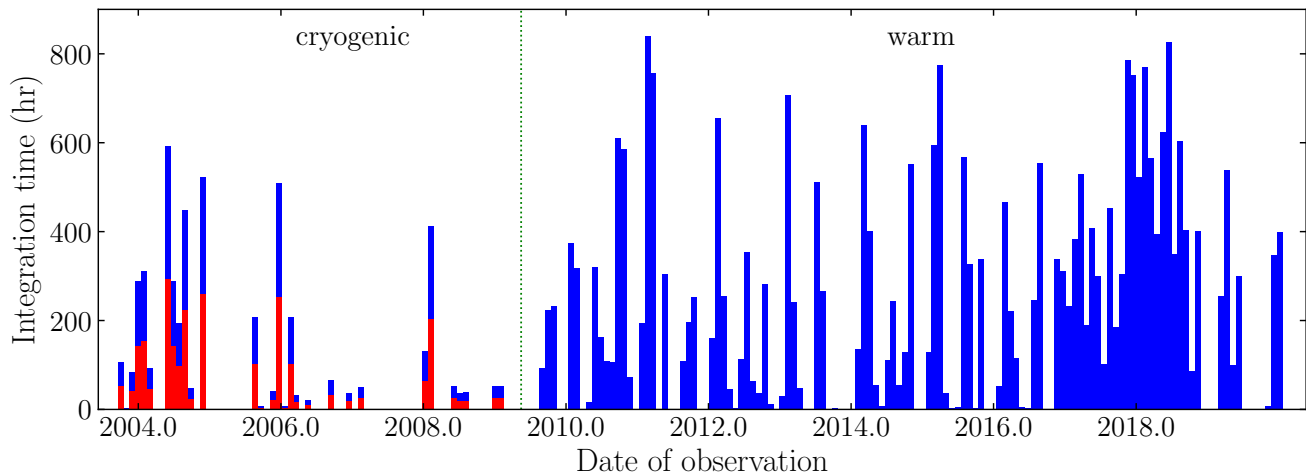


Fig. 1. Histogram of the exposure time of the data analysed here (including the few discarded observations) using bins of 30 days. Our dedicated observations began in November 2016 and comprise most of the data after that date. The red part of each bar accounts for observations in channels 3 and 4, and the blue part accounts for those in channels 1 and 2; the vertical dotted line at 2009.37 indicates the end of the cryogenic mission. No observations are made in channel 3 and 4 after the end of the cryogenic mission.

2. Observations

All observations described here were made with IRAC. In brief, IRAC is a four-channel array camera on the *Spitzer* Space Telescope, simultaneously observing four fields slightly separated on the sky at 3.6, 4.5, 5.8, and 8.0 μm , known as channels 1–4, respectively. *Spitzer* Space Telescope science observations began in August 2003, but observations in channels 3 and 4 ceased once the on-board cryogen was exhausted (May 15, 2009). During the following ‘warm mission’ phase, channels 1 and 2 continued to operate until the end of operations in late January 2020, albeit with somewhat lower, but still comparable, performance. The earliest observations presented here are archival observations that were obtained in September 2003; the observations of the dedicated Capak programme began in 2017, and the ones of the dedicated Scarlata programme began in 2019. The dedicated observations continued until January 2020, shortly before the shutdown of the satellite. Figure 1 shows a histogram of the integration time accumulated in bins of 30 days over the observing period. These observations account for almost 1.5 million frames, a total integration time of 34 000 h (all channels combined), and a total on-target time, omitting overheads, of just over 15 600 h, or nearly 1.8 yr, which is approximately 11% of the *Spitzer* Space Telescope mission time.

For our dedicated observations of EDF-N, EDF-S, and EDF-F we adopted a consistent observing strategy that comprises blocks of 3×3 maps with a step size of $310''$, a large three-point dither pattern, and four repeats per position. Each block covers a $15:1 \times 15:1$ region with a coverage of $3 \times 4 \times 100$ s exposures per pixel. The block centres are offset between passes in order to ensure uniform coverage and enable self-calibration. Each block forms an astronomical observation request (AOR), in IRAC jargon. All other data included in our processing are archival data. They were obtained with a variety of observing strategies that we did not investigate in detail and that we do not attempt to summarise here. In Appendix C, we list the programme IDs of all the observations processed; the ones of our dedicated observations are shown in bold. The combination of the archival data and our own dedicated data produces a spatially variable depth in most fields; this is discussed further in Sect. 4.

All observations are summarised in Table 1, which gives, for each field and channel, the number of frames (data collec-

tion events – DCEs – in IRAC terminology) used to produce the mosaics (we note that this can be lower than the number of frames downloaded as some were discarded; see Sect. 3) together with the total observing time. For channels 1 and 2, on the left side of the table, the information is sub-divided into the cryogenic part and the warm part of the mission.

3. Processing

3.1. Pre-processing and calibration

Processing begins with the *Level 1* data products generated by the *Spitzer* Science Center via their ‘basic calibrated data’ pipeline (Lowrance et al. 2016), which were downloaded from the NASA/IPAC Infrared Science Archive (IRSA²). They have had all well-understood instrumental signatures removed, have been flux-calibrated in units of MJy sr^{-1} , and are delivered with an uncertainty image and a mask image; they are described in detail in the IRAC Instrument Handbook³. More precisely, we begin from the ‘corrected basic calibration data’ products, which have file extensions `.cbcd` for the image, `.cbunc` for the uncertainty, and `.bimsk` for the mask. The files are grouped by AORs, namely sets of a few to several hundred DCEs obtained sequentially. All frames are 256×256 pixels, the pixels are $1''.2$ wide, and the image file header contains the photometric solution and an initial astrometric solution.

The processing was done region by region. A first pass over the files is used to check the headers for completeness and to discard a few incomplete AORs, which accounts for most of the differences in the number of frames listed in Table 1 between channels 1 and 2 or 3 and 4. This is followed by the correction of the ‘first frame’ bias effect⁴. Next, the positions and magnitudes of WISE (Wright et al. 2010; Mainzer et al. 2011) and *Gaia* DR2 (Gaia Collaboration 2018) sources falling within the field are downloaded. The *Gaia* sources are first ‘projected’ to their location at the time of the observations using the *Gaia*

² <https://irsa.ipac.caltech.edu>

³ <https://irsa.ipac.caltech.edu/data/SPITZER/docs/irac/iracinstrumenthandbook/home>

⁴ <https://irsa.ipac.caltech.edu/data/SPITZER/docs/irac/iracinstrumenthandbook/26/>

Table 1. Valid observations.

Field	Ch.	Cryo		Warm		Total		Ch.	Total	
		Num	Time (h)	Num	Time (h)	Num	Time (h)		Num	Time (h)
EDF-N	1	5859	52	113 521	2380	119 380	2432	3	5856	52
EDF-N	2	5857	52	113 204	2467	119 061	2519	4	7667	50
EDF-F	1	14 299	363	105 781	2672	120 080	3035	3	14 301	363
EDF-F	2	14 299	363	105 779	2764	120 078	3127	4	29 686	352
EDF-S	1	21 982	534	21 982	534	3
EDF-S	2	21 982	552	21 982	552	4
COSMOS	1	7014	185	191 072	4886	198 086	5071	3	7011	185
COSMOS	2	7013	185	191 031	5052	198 044	5237	4	13 894	179
EGS	1	4673	192	44 101	551	48 774	743	3	4 672	192
EGS	2	4673	192	44 101	569	48 774	761	4	14 535	186
HDFN	1	6253	298	36 485	930	42 738	1228	3	6252	298
HDFN	2	6253	298	36 485	962	42 738	1260	4	22 496	288
XMM	1	10 264	154	98 027	2410	108 291	2564	3	10 265	154
XMM	2	10 265	154	98 030	2495	108 295	2649	4	14 321	151

Notes. Here, ‘Num’ is the number of frames used, and ‘Time’ is the total integration time, in hours, they contribute. The left part of the table is for channels 1 and 2, split between cryogenic and warm mission, the right part is for channels 3 and 4, which were used during the cryogenic mission only. We note that the EDF-S field was observed only during the warm mission.

proper motions. Next, they are identified on each IRAC frame, their observed fluxes and positions are determined in each frame using the APEX software (the point-source extractor in MOPEX⁵) in forced-photometry mode, and the positions are used to update the astrometric solution of each frame. There are typically 30–40 *Gaia* DR2 sources available for each frame. In channels 1 and 2, most of them are detected and used for the astrometric correction. In the longer-wavelength channels, 3 and 4, only a few sources in total are detected and usable, but that is still sufficient to determine an astrometric solution with negligible distortion as shown in Sect. 4.2.

An attempt was made to subtract bright stars in order to recover faint sources in their wings. For each AOR, a model star built from the template PSFs described in the IRAC Instrument Handbook⁶ (see Fig. 4.9 there) is scaled to the median of the fluxes of the star measured in that AOR, and it is subtracted from each frame (of the AOR). Different templates are available for each filter and separately for the cryogenic and the warm missions. While this procedure worked quite well for moderately bright stars (which are of course the vast majority and which represent only a small loss in area), it introduced significant artefacts around the (few) very bright stars in the final mosaics. These artefacts included diffraction spikes corrected only out to a certain distance (out to where the template extends beyond the frame), other edge effects, and the subtraction of the core of bright galaxies. For these reasons, the bright-star subtraction was not performed and the bright stars are left as they are.

3.2. Stacking and image combination

In the next step, we computed a median image for all frames within an AOR, which corrects for persistence in the detectors and also for any residual first-frame pattern that introduces struc-

ture in the background. In parallel, a background map is also created by iteratively clipping objects and masking them, and finally that background is subtracted from each frame of the AOR.

The final processing steps consist of resampling the background-subtracted frames onto a common grid with a scale of $0''.6 \text{ pix}^{-1}$, that is, half the instrument pixel size, which covers all data in all channels and which is the same in all channels. We experimented with two MOPEX interpolation schemes to produce our final mosaics. We first tried the “drizzling” (Fruchter & Hook 2002) scheme in which the final value of the output pixels is computed by considering the contribution of each input pixel in a smaller pixel grid in the output image. This procedure has excellent noise properties (it does not suffer from correlated pixels) when many input frames are available, but with few input frames it can produce artefacts in the output images. The second, simpler approach is to compute the value of each output pixel as a linear combination of the input pixel values. Although this procedure produces correlated noise, it works reliably for all the fields considered in this work, which can have widely varying numbers of input images. Noise correlations can be estimated through simulations or by comparing sources in our drizzled and non-drizzled images. These comparisons show that the linear interpolation procedure leads to an underestimation of aperture magnitude errors by 30–40%, while the magnitudes themselves are unaffected.

Next, we used MOPEX to produce an average-combined image while rejecting outliers and excluding masked regions. Outlier rejection was done using the multi-frame temporal, dual outlier, and box outlier modules from MOPEX. We used the same parameters used by the *Spitzer* super mosaics, which were tuned to produce balanced outlier rejection for a wide range of data types and uses. The outlier rejection methods were then combined using the `MosaicRMASK` module. The specific parameters used can be found in Table 2. Frames with different exposure times are combined using the exposure time weighting feature in MOPEX. This appropriately scales the uncertainties and coverage maps to match the median exposure time before carrying out the combination.

⁵ <https://irsa.ipac.caltech.edu/data/SPITZER/docs/dataanalysis/tools/mopex/>

⁶ <https://irsa.ipac.caltech.edu/data/SPITZER/docs/irac/iracinstrumenthandbook/19/>

Table 2. MOPEX outlier rejection parameters.

Parameter name	Value
Temporal outlier: (&MOSAICOUTLIERIN)	
MIN_PIX_NUM	3
TOP_THRESHOLD	3.0
BOTTOM_THRESHOLD	3.0
THRESH_OPTION	1
Dual Outlier: (&MOSAICDUALOUTLIERIN)	
MAX_OUTL_FRAC	0.5
MAX_OUTL_IMAGE	1
Box Outlier: (&MOSAICBOXOUTLIERIN)	
BOX_Y	3
BOX_X	3
BOX_MEDIAN_BIAS	1
Mosaic RMASK: (&MOSAICRMASKIN)	
BOX_MIN_COVERAGE	1.0
BOX_BOTTOM_THRESHOLD	2.0
BOX_TOP_THRESHOLD	3.0
REFINE_OUTLIER_THRESH	1
REFINE_OUTLIER	0
RM_THRESH	0.5
MIN_COVERAGE	3
MAX_COVERAGE	100
TOP_THRESHOLD	3.0
BOTTOM_THRESHOLD	3.0

The stacking pipeline also produces the following ancillary characterisation maps: (1) an uncertainty map produced by stacking the input uncertainty maps using the same shifts as for the signal stack, (2) a coverage map giving the number of frames contributing to each pixel, and (3) an exposure time map giving the total exposure time per pixel. As the exposure times are not the same for all the observing programmes, these last two maps are not simply scaled versions of each other.

3.3. Spatial variation of the PSF in the stacks

The observations described here were made at many different satellite position angles (PAs), and thus when the images are stacked they must be rotated back to north upwards. This has the effect of rotating the PSF, which is fixed in the satellite’s reference frame. Since the PSF is not rotationally symmetric, due in particular to the diffraction spikes, the stacked image of a star will depend on when it was observed. As all parts of the stack were not observed at the same time (or at the same PA), the PSF varies spatially in the stack.

The COSMOS field, which is near the equator, was observable only at specific times and therefore with a very restricted range of PAs; the PSF in the COSMOS stacks is thus quite homogeneous. However, in the EDF-N, which was in a continuous viewing zone, observations were obtained at many different PAs, yielding a more complicated and more spatially variable PSF. This effect is very important for PSF-based photometry: the PSF at each position of the stack has to be reconstructed by stacking the nominal PSF at the PAs of the observations at that position, as did, for example, [Labbé et al. \(2015\)](#) for the GOODS-South and HUDF fields, and also [Weaver et al. \(2021, henceforth COSMOS2020\)](#) for the production of the COSMOS2020 catalogue. The latter used the PRFmap⁷ code by Andreas Faisst. While such

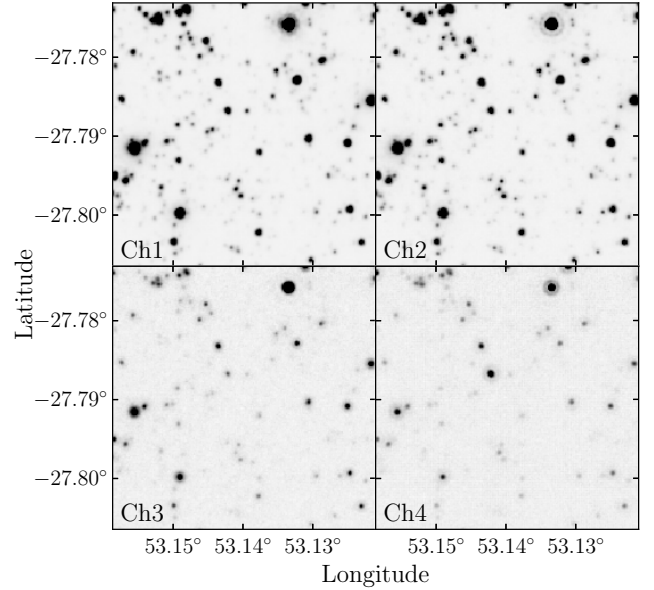


Fig. 2. Detail of EDF-F mosaic in region near that of maximum exposure time, which here is the same for all four channels. Images are 200×200 pixels, or $2' \times 2'$. Display levels are $-\sigma$ to $+8\sigma$, where σ is the standard deviation of the sky pixels, which is ~ 0.005 MJy sr^{-1} for channels 1 & 2, and ~ 0.013 MJy sr^{-1} for channels 3 & 4.

photometry is beyond the scope of this paper, we nevertheless provide, for each stack, a table of the PAs of each frame used in the stack. For completeness, those tables also contain the frame coordinates, the MJD of the observation, and the exposure time (see Appendix A for more details).

3.4. Products

As an example of the data quality, Fig. 2 shows a zoomed-in image of a section of the EDF-F mosaic in the four channels near the region of maximum coverage. We do not provide figures of the full mosaics here as they would be physically too small to show anything informative other than the overall coverage.

Maps of the integration time per pixel for channels 1 and 3 of all the fields are presented in Appendix B. Since channel 2 is observed together with channel 1, and similarly for channels 4 and 3, the paired channels have very similar coverage, albeit slightly shifted in position. The 10 deg^2 circular area of EDF-N and EDF-F and the 20 deg^2 pill-shaped area of EDF-S are easily seen in those figures. Also, and with the exception of EDF-S, for which there are only observations done specifically for this programme and no archival data, the integration time per pixel, and consequently the depth reached, is far from uniform, with only a small part of the total area of each field having been observed for more than a few hours. In fact, the median integration time per pixel is greater than 1 h for only two fields. Table 3 gives the median and maximum pixel integration time for each field and each channel.

The variation of area covered as a function of exposure time for channels 1 and 3 and for all fields is shown graphically in Fig. 3, which presents a cumulative histogram of the area covered versus exposure time. The intersection of the curve with the vertical axis thus gives the total area covered for that field and these areas are also listed in Table 4. EDF-S is the most uniformly observed field and it covers the largest area, but it is

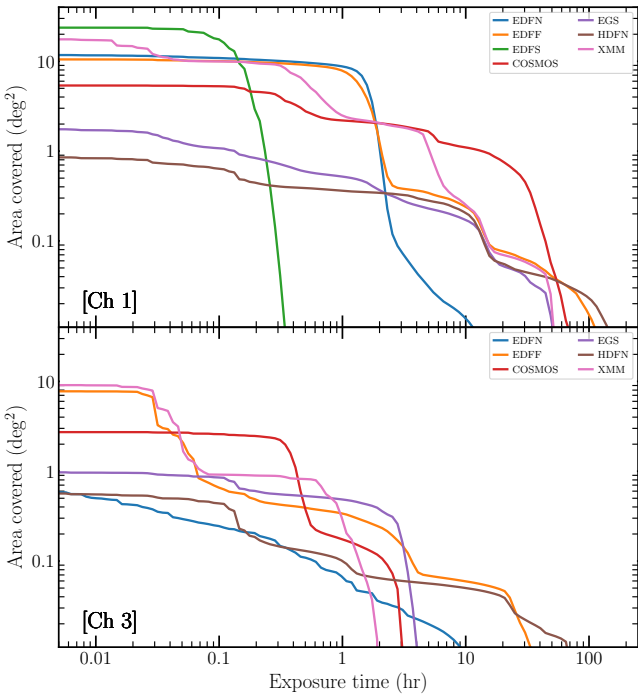
⁷ <https://github.com/cosmic-dawn/prfmap>

Table 3. Median and maximum pixel integration time in hours.

Field	ch1	ch2	ch3	ch4
COSMOS	0.51	93.7	0.50	97.1
EDF-F	1.33	199.7	1.33	149.5
EDF-N	1.47	23.4	1.56	21.3
EDF-S	0.13	0.5	0.16	0.5
EGS	0.16	71.1	0.16	71.6
HDFN	0.16	236.2	0.16	224.4
XMM	0.31	65.9	0.33	67.1

Table 4. Location and area, in deg², covered in each field.

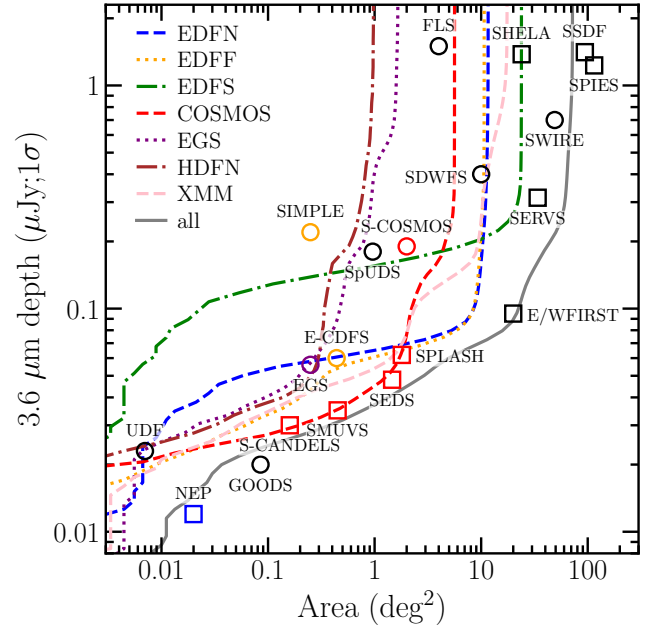
Field	RA	Dec	ch1	ch2	ch3	ch4
EDF-N	17 ^h 58 ^m	66°;36′	11.74	11.54	0.61	0.62
EDF-F	3 ^h 32 ^m	−28°12′	10.52	11.05	7.78	7.77
EDF-S	4 ^h 05 ^m	−48°30′	23.60	23.14
COSMOS	10 ^h 00 ^m	2°12′	5.37	5.46	2.72	2.72
EGS	14 ^h 19 ^m	52°42′	1.76	1.80	0.97	0.98
HDFN	12 ^h 37 ^m	62°24′	0.91	0.91	0.57	0.63
XMM	2 ^h 27 ^m	−4°36′	17.54	17.48	9.09	9.10


Fig. 3. Cumulative area coverage as a function of exposure time for channels 1 and 3, for all fields. The figures for channels 2 and 4 are similar to the ones above, as explained in the text.

also the shallowest, with only 0.1 h per pixel on average, and it is also the only field with no channel 3 and 4 data. EDF-F and EDF-N reach the target coverage of 10 deg² with about 1 h of exposure time, with the latter showing deeper coverage over smaller zones. The other fields were covered by many observing programmes with different objectives and which covered specific areas to different depths. The combination of these programmes with our own yields a curve with many plateaus. Finally, there are a few small parts of the EDF-F and HDFN fields that have more than 100 h of exposure time.

3.5. Final sensitivities

We estimated the sensitivities of the stacked images by measuring the flux in circular 2''5 diameter apertures randomly placed across each image after masking the regions with detected objects using the SExtractor (Bertin & Arnouts 1996) segmentation map. The sensitivity is then computed as the standard deviation of these fluxes (3 σ clipped). This procedure is done in 200 × 200 pixel cells (4 arcmin²). Figure 4 shows the cumulative area covered as a function of sensitivity for the channel


Fig. 4. Sensitivity of *Spitzer*/IRAC channel 1 data as a function of cumulative area coverage. The coloured lines illustrate 1 σ depths measured in empty 2''5 diameter apertures in each field. The grey solid line is the total area observed to a given depth summed over different surveys. The data points indicate point-source sensitivities at 1 σ compiled in Ashby et al. (2018) (we note that some of these data are included in our stacks). The circles and squares represent surveys executed during cryogenic and warm missions, respectively.

1 mosaics. We note the similarity between this figure and the top panel of Fig. 3 once the latter is rotated by 90 degrees. The solid line shows our total depth, summed over all our survey fields. Also shown in the figure are the published sensitivities of the surveys that are included in our data and analyses. Generally, our measured sensitivities are consistent with literature measurements for surveys of equivalent exposure time.

4. Validation and quality control

As part of our validation process, we compare photometry and astrometry of sources in our stacks with reference catalogues and also extract number counts that can be compared to previous works.

4.1. Catalogue extraction

We began by extracting source catalogues from channel 1 and 2 stacks of all fields using SExtractor. We adopted the usual

Table 5. SExtractor parameters used for detection and photometry.

Parameter name	Value
DETECT_MINAREA	5
DETECT_MAXAREA	1000000
THRESH_TYPE	RELATIVE
DETECT_THRESH	2
ANALYSIS_THRESH	2
FILTER_NAME	gauss_2.5_5x5.conv
DEBLEND_NTHRESH	32
DEBLEND_MINCONT	0.00001
BACK_SIZE	32
BACKPHOTO_THICK	32
BACK_FILTERSIZE	3
BACKPHOTO_TYPE	LOCAL
MAG_ZEROPOINT	21.58
PHOT_AUTOPARAMS	2.5,5.0
PIXEL_SCALE	0.60

approach of searching for objects that contain a minimum number of connected pixels above a specified noise threshold (in this case 2σ) and measuring their aperture magnitudes. In the case of our moderately deep IRAC data, where many sources are blended due to the large IRAC PSF, this approach is known to miss faint sources. However, these faint sources are not required for our quality assessment purposes and a shallower catalogue is entirely sufficient. SExtractor estimates a global background on a grid with mesh size of 32×32 pixels (we remind the reader that pixels are $0''.6$ wide). This background is smoothed with a 5×5 pixel Gaussian kernel with a FWHM = $1''.5$. For each source, the flux is measured within a circular aperture of $7''$ diameter, and a local background is estimated within an annulus of width 32 pixels around the isophotal limits. The measured fluxes were converted from MJy/sr to AB magnitude using a zero-point of 21.58 (which accounts for a zero-magnitude flux of 3631 Jy and a pixel size of $0''.6$ ⁸), and the latter were converted to total magnitude using the aperture corrections given in the IRAC Instrument Handbook for the warm mission (-0.1164 and -0.1158 for channel 1 and channel 2, respectively), which covers the vast majority of the data, while the correction for the cryogenic mission differs at only the 1–2% level⁹. A list of relevant SExtractor parameters used for the catalogue extraction can be found in Table 5.

4.2. Astrometric and photometric validation

Using the catalogues extracted above, we evaluated the astrometric accuracy of our stacked images. For each field, we cross-matched sources with magnitude $16 < [3.6] < 19$ within $1''$ of their counterparts in the *Gaia* DR2 catalogue. This magnitude range was adopted to ensure that only bright, non-blended sources were chosen. We now present a detailed analysis for EDF-N, but other fields are similar.

Figure 5 shows the difference between reference and measured coordinates (for clarity, only one point in ten is shown). The heavy blue dashed line gives the size of one pixel in the

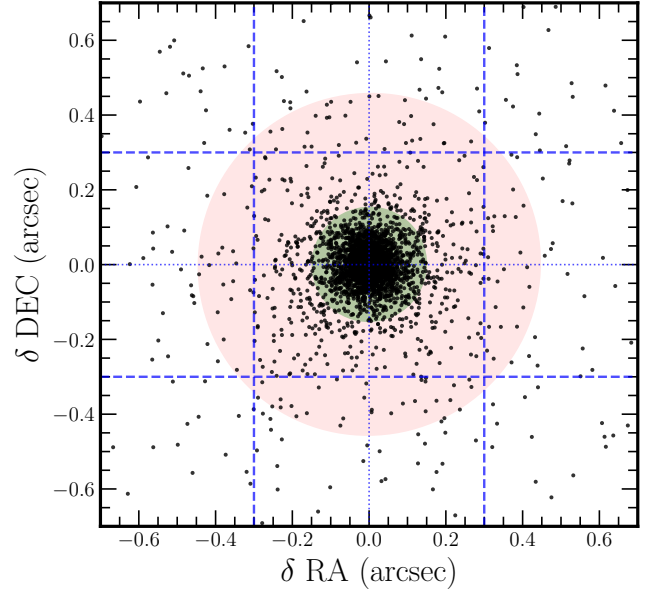


Fig. 5. Difference between the reference and the measured position, in arcseconds, of *Gaia* DR2 catalogue sources with $16 < [3.6] < 19$ total magnitudes extracted from the EDF-N channel 1 mosaic. The blue dashed lines indicate the size of one mosaic pixel. The blue dotted lines go through the origin. The shaded regions are ellipses containing 68% and 99% of all sources, respectively. For clarity, only one in ten sources is plotted.

stacked image (which is half the size of the instrument pixel). Similarly (again showing only one in ten points), Fig. 6 shows, for each coordinate, the difference between the reference and the measured value as a function of position along the other coordinate. The thick red dashed line shows a running median computed over a bin containing 20 points. The flatness of this line indicates that there is no significant spatial variation in astrometric precision. Considering all fields, we find that the 1σ precision (measured as the RMS of the difference between positions in our catalogue and those in *Gaia* DR2) is $0''.15$. Furthermore, the median value is always $\leq 0''.1$, with the exception of the sparsely-covered HDF-N field where it is $\leq 0''.2$. These measurements demonstrate that the astrometric solutions have been correctly applied to the individual images and that the combined images are free of residuals on a scale much smaller than an individual mosaic pixel, which is more than sufficient to measure precise infrared and optical-infrared colours.

Finally, we perform a simple check on the photometric calibration of our mosaics. As described previously, individual images are photometrically calibrated by the *Spitzer* Science Center (SSC). Following the validation procedures outlined by the SSC, we compare magnitudes of objects in our catalogues with those in the WISE survey. Because of the difference between the WISE W1 and IRAC channel 1 filter profiles, we selected objects with $[3.6] - [4.5] \sim 0$. Figure 7 shows the magnitude difference for the EDF-N field, and the agreement is excellent. Further comparisons with photometric measurements in previous COSMOS IRAC surveys can be found in the appendix of COSMOS2020.

4.3. Magnitude number counts

We computed the differential number counts in channel 1 of each field using the corrected $7''$ aperture magnitudes. Since

⁸ <https://irsa.ipac.caltech.edu/data/SPITZER/docs/irac/iracinstrumenthandbook/19/>

⁹ https://irsa.ipac.caltech.edu/data/SPITZER/docs/irac/calibrationfiles/ap_corr_warm/

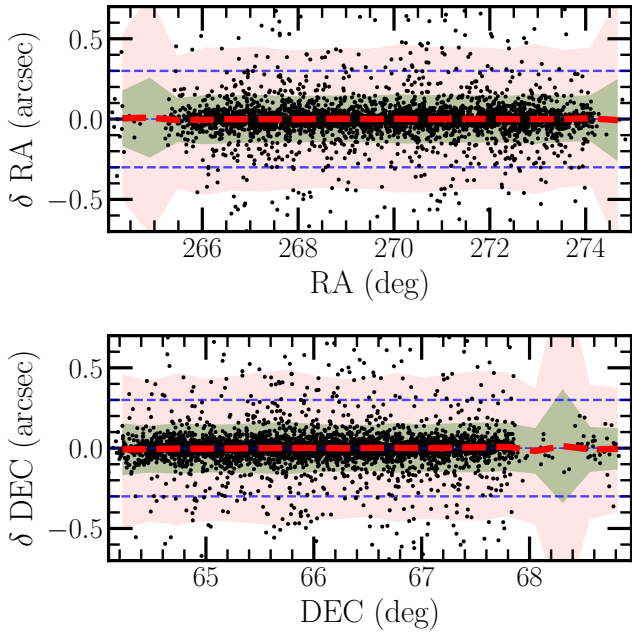


Fig. 6. Difference between the reference *Gaia* DR2 catalogue and the measured RA (*top panel*) and Dec (*bottom panel*) of sources in the EDF-N channel 1 mosaic with $16 < [3.6] < 19$ total magnitudes as a function of the coordinate. The solid red line shows a running median computed in bins of 20 points, and the shaded areas indicate the regions containing 68% and 99% of all sources, respectively.

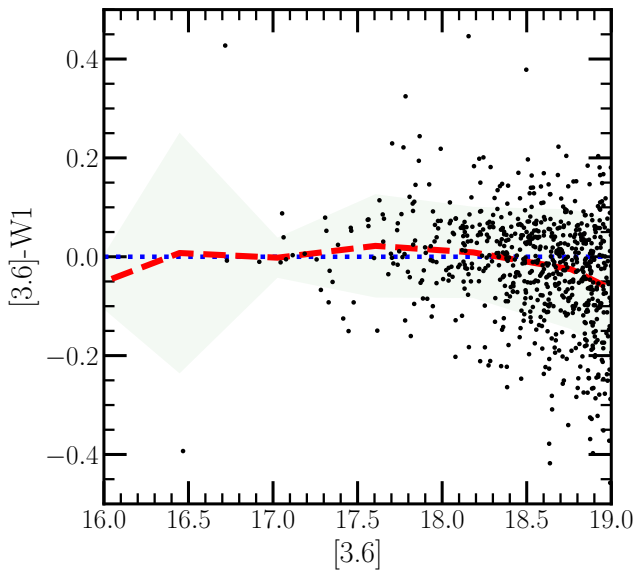


Fig. 7. Photometric comparison with WISE survey. The magnitude measured in $7''$ apertures for flat-spectrum objects ($[3.6]-[4.5] \sim 0$) is compared with W1 magnitudes in the ALLWISE survey. The shaded area represents the 68% confidence interval.

the IRAC PSF is too large to perform morphological source classification, we simply included all objects detected. These are shown in Fig. 8, where the red circles with uncertainties present our measurements, and the lines show the number counts from the literature; the bottom-right panel shows the mean of all fields. We compared our number counts with those presented in [Ashby et al. \(2013\)](#), which also surveyed many of our fields and with those computed using the new COSMOS2020

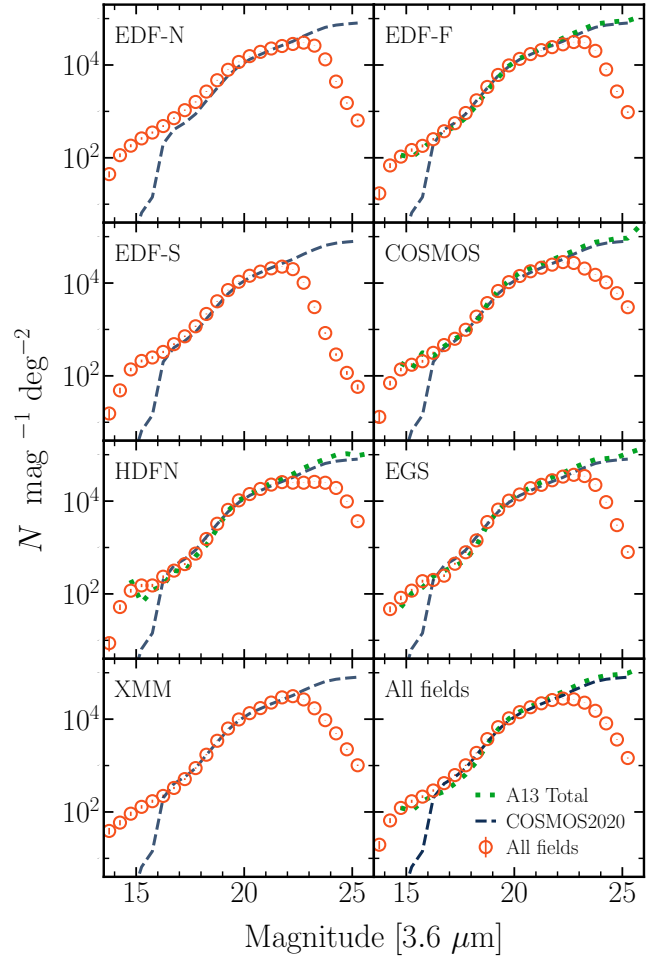


Fig. 8. Magnitude number counts in channel 1 (red circles) together with COSMOS2020 (long dashed lines) and [Ashby et al. \(2013\)](#), hereafter A13; short dotted green lines). *Bottom right panel*: mean of all fields, and the legend there applies to all panels.

photometric catalogue (COSMOS2020) that we used as the reference.

There is a general agreement in the number counts in all the fields with [Ashby et al. \(2013\)](#) and COSMOS2020 for $16 < [3.6] < 22$. At brighter magnitudes, the COSMOS2020 counts drop off as bright sources were not included. At fainter magnitudes, our aperture-based catalogues are confusion-limited and thus incomplete. Conversely, the COSMOS2020 catalogue, which uses a high-resolution prior for the detection and a profile-fitting method for the measurement, is complete up to significantly fainter magnitudes.

Counts for EDF-N are slightly higher than the other fields at bright magnitudes. To investigate this difference, we simulated a stellar catalogue of 1 deg^2 centred on EDF-N using TRILEGAL ([Girardi et al. 2005](#)) and compared counts from this simulated catalogue with our observations, shown in Fig. 9. At bright magnitudes, where stars are expected to outnumber galaxies, our counts are in reasonable agreement with TRILEGAL predictions, and in excellent agreement with the number counts extracted from the AllWISE ([Wright et al. 2010](#)) catalogue for this field. These comparisons indicate that the difference between EDF-N and other fields is largely due to the higher density of stellar sources in there, which is consistent with its lower Galactic latitude.

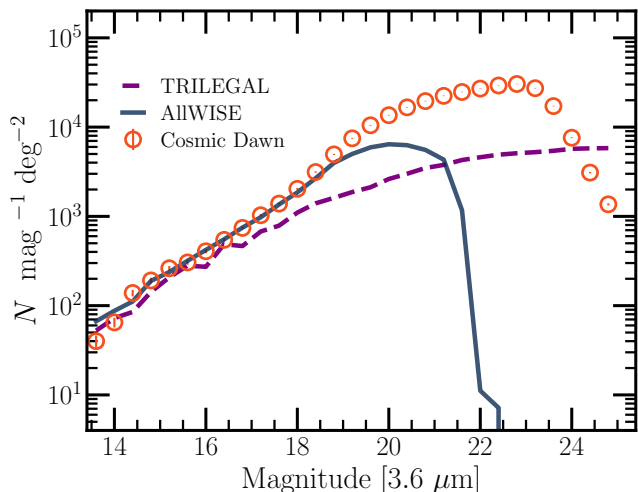


Fig. 9. Magnitude number counts in EDF-N field compared to AllWISE and predicted stellar number counts from TRILEGAL.

5. Summary

We have presented the *Spitzer* Space Telescope/IRAC mid-infrared component of the Cosmic Dawn Survey: an effort to complement the *Euclid* mission’s observations of deep and calibration fields with deep longer-wavelength data to enable high redshift legacy science.

The survey consists of two major new programmes covering the three *Euclid* deep fields (EDF-N, EDF-F and EDF-S) and a homogeneous reprocessing of all existing data in *Euclid*’s four calibration fields (COSMOS, XMM, EGS and HDFN). We have processed new data together with all relevant archival data to produce mosaics of these fields covering a total of $\sim 71 \text{ deg}^2$ in IRAC channels 1 and 2. Furthermore, the new mosaics are tied to the *Gaia* astrometric reference system. The MIR data will be essential for a wide range of legacy science with *Euclid*, including improved star/galaxy separation, more accurate photometric redshifts, determination of stellar masses of galaxies, and the construction of complete galaxy samples at $z > 2$ with well understood selection effects.

We validated our final products by comparing catalogues extracted from channels 1 and 2 to external catalogues. In all fields, comparing with *Gaia* DR2, the residual astrometric uncertainty for sources with total magnitudes $16 < [3.6] < 19$ is around $0''.15 (1\sigma)$. Our photometric measurements are in excellent agreement with WISE photometry and our number counts are consistent with previous determinations.

The Cosmic Dawn Survey *Spitzer* Space Telescope survey presented here represents the first essential step in assembling the required multi-wavelength coverage in the *Euclid* deep fields which are set to become some of the most important fields in extragalactic astronomy for the coming decade. Since the *Spitzer* Space Telescope mission has finished, and all available data in these fields have been processed with the latest reduction pipeline, the resulting mosaics will remain the deepest and widest MIR imaging survey for the foreseeable future. No existing or approved future observatories are capable of obtaining such data. While JWST is more sensitive and has higher spatial resolution at these wavelengths, its mapping speed is too slow to cover comparable degree-scale areas.

In the context of the Cosmic Dawn Survey, several programmes are currently underway to add data at other wavelengths to the *Euclid* deep fields and calibration fields. In

particular deep optical data in the EDF-N and EDF-F are currently being obtained with the Subaru’s Hyper-Suprime-Cam instrument as part of the Hawaii-Two-0 observing programme (McPartland et al., in prep.). These fields are also being targeted with high spatial resolution millimeter observations as part of the planned Large-scale Structure Survey with the Toltech Camera¹⁰ on the Large Millimeter Telescope (LMT, Pope et al. 2019). A deep *U*-band survey is also underway with the CFHT (Zalesky et al., in prep.). EDF-S is being covered with *K*-band observations from the VISTA telescope (Nonino et al., priv. comm.), and planning is ongoing to obtain optical data with the *Vera C. Rubin* Observatory.

The Cosmic Dawn Survey *Spitzer* Space Telescope mosaics and associated products described here can be downloaded from the IRSA web site, Appendix A gives the details of the download site and the naming convention used. The community is encouraged to make use of them for their science.

Acknowledgements. We thank the MOPEX support team for fixing issues that appeared when combining large numbers of files. This publication is based on observations made with the *Spitzer* Space Telescope, which is operated by the Jet Propulsion Laboratory, California Institute of Technology under a contract with NASA, and has made use of the NASA/IPAC Infrared Science Archive, which is funded by the National Aeronautics and Space Administration and operated by the California Institute of Technology. This publication has also made use of data from the European Space Agency (ESA) mission *Gaia* (<https://www.cosmos.esa.int/gaia>), processed by the *Gaia* Data Processing and Analysis Consortium (DPAC, <https://www.cosmos.esa.int/web/gaia/dpac/consortium>). Funding for the *Gaia* Data Processing and Analysis Consortium (DPAC) has been provided by national institutions, in particular the institutions participating in the *Gaia* Multilateral Agreement. This publication makes use of data products from the Wide-field Infrared Survey Explorer (WISE), which is a joint project of the University of California, Los Angeles, and the Jet Propulsion Laboratory/California Institute of Technology, funded by the National Aeronautics and Space Administration. H.J.McC. acknowledges support from the PNCG. This work used the CANDIDE computer system at the IAP supported by grants from the PNCG and the DIM-ACAV and maintained by S. Rouberol. S.T. and J.W. acknowledge support from the European Research Council (ERC) Consolidator Grant funding scheme (project ConTESt, grant No. 648179). I.D. has received funding from the European Union’s Horizon 2020 research and innovation programme under the Marie Skłodowska-Curie grant agreement No. 896225. The Cosmic Dawn Center is funded by the Danish National Research Foundation under grant No. 140. H. Hildebrandt is supported by a Heisenberg grant of the Deutsche Forschungsgemeinschaft (Hi 1495/5-1) as well as an ERC Consolidator Grant (No. 770935). The *Euclid* Consortium acknowledges the European Space Agency and a number of agencies and institutes that have supported the development of *Euclid*, in particular the Academy of Finland, the Agenzia Spaziale Italiana, the Belgian Science Policy, the Canadian *Euclid* Consortium, the French Centre National d’Etudes Spatiales, the Deutsches Zentrum für Luft-und Raumfahrt, the Danish Space Research Institute, the Fundação para a Ciência e a Tecnologia, the Ministerio de Ciencia e Innovación, the National Aeronautics and Space Administration, the National Astronomical Observatory of Japan, the Nederlandse Onderzoekschool Voor Astronomie, the Norwegian Space Agency, the Romanian Space Agency, the State Secretariat for Education, Research and Innovation (SERI) at the Swiss Space Office (SSO), and the United Kingdom Space Agency. A complete and detailed list is available on the *Euclid* web site (<http://www.euclid-ec.org>).

References

- Aihara, H., Allende Prieto, C., An, D., et al. 2011, *ApJS*, 193, 29
- Ashby, M. L. N., Willner, S. P., Fazio, G. G., et al. 2013, *ApJ*, 769, 80
- Ashby, M. L. N., Caputi, K. I., Cowley, W., et al. 2018, *ApJS*, 237, 39
- Beckwith, S. V. W., Stiavelli, M., Koekemoer, A. M., et al. 2006, *AJ*, 132, 1729
- Bell, E. F., & de Jong, R. S. 2001, *ApJ*, 550, 212
- Bertin, E., & Arnouts, S. 1996, *A&AS*, 117, 393
- Bouwens, R. J., Stefanon, M., Oesch, P. A., et al. 2019, *ApJ*, 880, 25
- Bowler, R. A. A., Jarvis, M. J., Dunlop, J. S., et al. 2020, *MNRAS*, 493, 2059
- Brammer, G. B., van Dokkum, P. G., Franx, M., et al. 2012, *ApJS*, 200, 13
- Bridge, J. S., Holwerda, B. W., Stefanon, M., et al. 2019, *ApJ*, 882, 42

¹⁰ <http://toltec.astro.umass.edu/>

- Caputi, K. I., Ilbert, O., Laigle, C., et al. 2015, *ApJ*, **810**, 73
- Davidzon, I., Ilbert, O., Laigle, C., et al. 2017, *A&A*, **605**, A70
- Fruchter, A. S., & Hook, R. N. 2002, *PASP*, **114**, 144
- Gaia Collaboration (Brown, A. G. A., et al.) 2018, *A&A*, **616**, A1
- Giavalisco, M., Ferguson, H. C., Koekemoer, A. M., et al. 2004, *ApJ*, **600**, L93
- Girardi, L., Groenewegen, M. A. T., Hatziminaoglou, E., & da Costa, L. 2005, *A&A*, **436**, 895
- Grogin, N. A., Kocevski, D. D., Faber, S. M., et al. 2011, *ApJS*, **197**, 35
- Kauffmann, O. B., Le Fèvre, O., Ilbert, O., et al. 2020, *A&A*, **640**, A67
- Labbé, I., Oesch, P. A., Illingworth, G. D., et al. 2015, *ApJS*, **221**, 23
- Lacy, M., Surace, J. A., Farrah, D., et al. 2021, *MNRAS*, **501**, 892
- Laureijs, R., Amiaux, J., Arduini, S., et al. 2011, ArXiv e-prints [arXiv:1110.3193]
- Le Fèvre, O., Tasca, L. A. M., Cassata, P., et al. 2015, *A&A*, **576**, A79
- Lérand, L., McCracken, H. J., Davidzon, I., et al. 2019, *MNRAS*, **486**, 5468
- Lonsdale, C. J., Smith, H. E., Rowan-Robinson, M., et al. 2003, *PASP*, **115**, 897
- Lowrance, P. J., Carey, S. J., Surace, J. A., et al. 2016, in *Space Telescopes and Instrumentation 2016: Optical, Infrared, and Millimeter Wave*, eds. H. A. MacEwen, G. G. Fazio, M. Lystrup, et al., *SPIE*, **9904**, 1853
- Mainzer, A., Grav, T., Bauer, J., et al. 2011, *ApJ*, **743**, 156
- Mauduit, J.-C., Lacy, M., Farrah, D., et al. 2012, *PASP*, **124**, 714
- Moneti, A., McCracken, H. J., Rouberol, S., et al. 2019, *The Fourth UltraVISTA data release*, *ESO*
- Pérez-González, P. G., Rieke, G. H., Villar, V., et al. 2008, *ApJ*, **675**, 234
- Pope, A., Aretxaga, I., Hughes, D., Wilson, G., & Yun, M. 2019, *Am. Astron. Soc. Meeting Abstracts*, **233**, 363.20
- Sanders, D. B., Salvato, M., Aussel, H., et al. 2007, *ApJS*, **172**, 86
- Scoville, N., Aussel, H., Brusa, M., et al. 2007, *ApJS*, **172**, 1
- Trac, H., Cen, R., & Loeb, A. 2008, *ApJ*, **689**, L81
- Weaver, J. R., Kauffmann, O. B., Ilbert, O., et al. 2021, *ApJS*, **258**, 11
- Werner, M. W., Roellig, T. L., Low, F. J., et al. 2004, *ApJS*, **154**, 1
- Wright, E. L., Eisenhardt, P. R. M., Mainzer, A. K., et al. 2010, *AJ*, **140**, 1868
- ¹ Institut d'Astrophysique de Paris, 98bis Boulevard Arago, 75014, Paris, France
e-mail: moneti@iap.fr
- ² Sorbonne Universités, UPMC Univ Paris 6 et CNRS, UMR 7095, Institut d'Astrophysique de Paris, 98 bis bd Arago, 75014 Paris, France
- ³ Aix-Marseille Univ, CNRS, CNES, LAM, Marseille, France
- ⁴ Cosmic Dawn Center (DAWN), Niels Bohr Institute, University of Copenhagen, Vibenshuset, Lyngbyvej 2, 2100 Copenhagen, Denmark
- ⁵ Minnesota Institute for Astrophysics, University of Minnesota, 116 Church St SE, Minneapolis, MN 55455, USA
- ⁶ Cosmic Dawn Center (DAWN), Copenhagen, Denmark
- ⁷ Niels Bohr Institute, University of Copenhagen, Jagtvej 128, 2200 Copenhagen, Denmark
- ⁸ Infrared Processing and Analysis Center, California Institute of Technology, Pasadena, CA 91125, USA
- ⁹ California Institute of Technology, 1200 E California Blvd, Pasadena, CA 91125, USA
- ¹⁰ Physics and Astronomy Department, University of California, 900 University Ave., Riverside, CA 92521, USA
- ¹¹ Institute for Astronomy, University of Hawaii, 2680 Woodlawn Drive, Honolulu, HI 96822, USA
- ¹² INFN-Sezione di Roma, Piazzale Aldo Moro, 2 – c/o Dipartimento di Fisica, Edificio G. Marconi, 00185 Roma, Italy
- ¹³ INAF-Osservatorio Astronomico di Roma, Via Frascati 33, 00078 Monteporzio Catone, Italy
- ¹⁴ Jet Propulsion Laboratory, California Institute of Technology, 4800 Oak Grove Drive, Pasadena, CA 91109, USA
- ¹⁵ Institute of Cosmology and Gravitation, University of Portsmouth, Portsmouth PO1 3FX, UK
- ¹⁶ INAF-Osservatorio di Astrofisica e Scienza dello Spazio di Bologna, Via Piero Gobetti 93/3, 40129 Bologna, Italy
- ¹⁷ Max Planck Institute for Extraterrestrial Physics, Giessenbachstr. 1, 85748 Garching, Germany
- ¹⁸ INAF-Osservatorio Astrofisico di Torino, Via Osservatorio 20, 10025 Pino Torinese, TO, Italy
- ¹⁹ INFN-Sezione di Roma Tre, Via della Vasca Navale 84, 00146 Roma, Italy
- ²⁰ Department of Mathematics and Physics, Roma Tre University, Via della Vasca Navale 84, 00146 Rome, Italy
- ²¹ Institut de Recherche en Astrophysique et Planétologie (IRAP), Université de Toulouse, CNRS, UPS, CNES, 14 Av. Edouard Belin, 31400 Toulouse, France
- ²² INAF-Osservatorio Astronomico di Capodimonte, Via Moiriello 16, 80131 Napoli, Italy
- ²³ Centro de Astrofísica da Universidade do Porto, Rua das Estrelas, 4150-762 Porto, Portugal
- ²⁴ Instituto de Astrofísica e Ciências do Espaço, Universidade do Porto, CAUP, Rua das Estrelas, 4150-762 Porto, Portugal
- ²⁵ INAF-IASF Milano, Via Alfonso Corti 12, 20133 Milano, Italy
- ²⁶ Port d'Informació Científica, Campus UAB, C. Albareda s/n, 08193 Bellaterra, Barcelona, Spain
- ²⁷ Institut de Física d'Altes Energies (IFAE), The Barcelona Institute of Science and Technology, Campus UAB, 08193 Bellaterra, Barcelona, Spain
- ²⁸ Institute of Space Sciences (ICE, CSIC), Campus UAB, Carrer de Can Magrans, s/n, 08193 Barcelona, Spain
- ²⁹ Institut d'Estudis Espacials de Catalunya (IEEC), Carrer Gran Capitá 2-4, 08034 Barcelona, Spain
- ³⁰ Department of Physics “E. Pancini”, University Federico II, Via Cinthia 6, 80126 Napoli, Italy
- ³¹ INFN section of Naples, Via Cinthia 6, 80126 Napoli, Italy
- ³² Dipartimento di Fisica e Astronomia “Augusto Righi” – Alma Mater Studiorum Università di Bologna, Viale Berti Pichat 6/2, 40127 Bologna, Italy
- ³³ INAF-Osservatorio Astrofisico di Arcetri, Largo E. Fermi 5, 50125 Firenze, Italy
- ³⁴ Institut national de physique nucléaire et de physique des particules, 3 rue Michel-Ange, 75794 Paris Cédex 16, France
- ³⁵ Centre National d'Etudes Spatiales, Toulouse, France
- ³⁶ Institute for Astronomy, University of Edinburgh, Royal Observatory, Blackford Hill, Edinburgh EH9 3HJ, UK
- ³⁷ Jodrell Bank Centre for Astrophysics, School of Physics and Astronomy, University of Manchester, Oxford Road, Manchester M13 9PL, UK
- ³⁸ European Space Agency/ESRIN, Largo Galileo Galilei 1, 00044 Frascati, Roma, Italy
- ³⁹ ESAC/ESA, Camino Bajo del Castillo, s/n., Urb. Villafranca del Castillo, 28692 Villanueva de la Cañada, Madrid, Spain
- ⁴⁰ Univ Lyon, Univ Claude Bernard Lyon 1, CNRS/IN2P3, IP2I Lyon, UMR 5822, 69622, Villeurbanne, France
- ⁴¹ Mullard Space Science Laboratory, University College London, Holmbury St Mary, Dorking, Surrey RH5 6NT, UK
- ⁴² Departamento de Física, Faculdade de Ciências, Universidade de Lisboa, Edifício C8, Campo Grande, 1749-016 Lisboa, Portugal
- ⁴³ Instituto de Astrofísica e Ciências do Espaço, Faculdade de Ciências, Universidade de Lisboa, Campo Grande, 1749-016 Lisboa, Portugal
- ⁴⁴ Department of Astronomy, University of Geneva, ch. d'Ecogia 16, 1290 Versoix, Switzerland
- ⁴⁵ Université Paris-Saclay, CNRS, Institut d'astrophysique spatiale, 91405 Orsay, France
- ⁴⁶ Department of Physics, Oxford University, Keble Road, Oxford OX1 3RH, UK
- ⁴⁷ INFN-Padova, Via Marzolo 8, 35131 Padova, Italy
- ⁴⁸ AIM, CEA, CNRS, Université Paris-Saclay, Université de Paris, 91191 Gif-sur-Yvette, France
- ⁴⁹ INAF-Osservatorio Astronomico di Trieste, Via G. B. Tiepolo 11, 34131 Trieste, Italy
- ⁵⁰ Istituto Nazionale di Astrofisica (INAF) – Osservatorio di Astrofisica e Scienza dello Spazio (OAS), Via Gobetti 93/3, 40127 Bologna, Italy
- ⁵¹ Istituto Nazionale di Fisica Nucleare, Sezione di Bologna, Via Irnerio 46, 40126 Bologna, Italy
- ⁵² INAF-Osservatorio Astronomico di Brera, Via Brera 28, 20122 Milano, Italy
- ⁵³ INAF-Osservatorio Astronomico di Padova, Via dell'Osservatorio 5, 35122 Padova, Italy

- ⁵⁴ Universitäts-Sternwarte München, Fakultät für Physik, Ludwig-Maximilians-Universität München, Scheinerstrasse 1, 81679 München, Germany
- ⁵⁵ Institute of Theoretical Astrophysics, University of Oslo, PO Box 1029 Blindern, 0315 Oslo, Norway
- ⁵⁶ Leiden Observatory, Leiden University, Niels Bohrweg 2, 2333, CA Leiden, The Netherlands
- ⁵⁷ von Hoerner & Sulger GmbH, Schloßplatz 8, 68723 Schwetzingen, Germany
- ⁵⁸ Max-Planck-Institut für Astronomie, Königstuhl 17, 69117 Heidelberg, Germany
- ⁵⁹ Aix-Marseille Univ, CNRS/IN2P3, CPPM, Marseille, France
- ⁶⁰ Université de Genève, Département de Physique Théorique and Centre for Astroparticle Physics, 24 quai Ernest-Ansermet, 1211 Genève 4, Switzerland
- ⁶¹ Department of Physics and Helsinki Institute of Physics, Gustaf Hällströmin katu 2, 00014 University of Helsinki, Finland
- ⁶² NOVA optical infrared instrumentation group at ASTRON, Oude Hoogeveensedijk 4, 7991PD Dwingeloo, The Netherlands
- ⁶³ Argelander-Institut für Astronomie, Universität Bonn, Auf dem Hügel 71, 53121 Bonn, Germany
- ⁶⁴ Dipartimento di Fisica e Astronomia “Augusto Righi” – Alma Mater Studiorum Università di Bologna, Via Piero Gobetti 93/2, 40129 Bologna, Italy
- ⁶⁵ INFN-Sezione di Bologna, Viale Berti Pichat 6/2, 40127 Bologna, Italy
- ⁶⁶ Centre for Extragalactic Astronomy, Department of Physics, Durham University, South Road, Durham DH1 3LE, UK
- ⁶⁷ Université Côte d’Azur, Observatoire de la Côte d’Azur, CNRS, Laboratoire Lagrange, Bd de l’Observatoire, CS 34229, 06304 Nice cedex 4, France
- ⁶⁸ Institute of Physics, Laboratory of Astrophysics, Ecole Polytechnique Fédérale de Lausanne (EPFL), Observatoire de Sauverny, 1290 Versoix, Switzerland
- ⁶⁹ European Space Agency/ESTEC, Keplerlaan 1, 2201 AZ Noordwijk, The Netherlands
- ⁷⁰ Department of Physics and Astronomy, University of Aarhus, Ny Munkegade 120, 8000 Aarhus C, Denmark
- ⁷¹ Institute of Space Science, Bucharest 077125, Romania
- ⁷² Departamento de Astrofísica, Universidad de La Laguna, 38206 La Laguna, Tenerife, Spain
- ⁷³ Instituto de Astrofísica de Canarias, Calle Vía Láctea s/n, 38204 San Cristóbal de La Laguna, Tenerife, Spain
- ⁷⁴ Dipartimento di Fisica e Astronomia “G.Galilei”, Università di Padova, Via Marzolo 8, 35131 Padova, Italy
- ⁷⁵ Centro de Investigaciones Energéticas, Medioambientales y Tecnológicas (CIEMAT), Avenida Complutense 40, 28040 Madrid, Spain
- ⁷⁶ Instituto de Astrofísica e Ciências do Espaço, Faculdade de Ciências, Universidade de Lisboa, Tapada da Ajuda, 1349-018 Lisboa, Portugal
- ⁷⁷ Universidad Politécnica de Cartagena, Departamento de Electrónica y Tecnología de Computadoras, 30202 Cartagena, Spain
- ⁷⁸ INFN-Sezione di Torino, Via P. Giuria 1, 10125 Torino, Italy
- ⁷⁹ Dipartimento di Fisica, Università degli Studi di Torino, Via P. Giuria 1, 10125 Torino, Italy
- ⁸⁰ Université de Paris, CNRS, Astroparticule et Cosmologie, 75013 Paris, France
- ⁸¹ Space Science Data Center, Italian Space Agency, Via del Politecnico snc, 00133 Roma, Italy
- ⁸² IFPU, Institute for Fundamental Physics of the Universe, Via Beirut 2, 34151 Trieste, Italy
- ⁸³ SISSA, International School for Advanced Studies, Via Bonomea 265, 34136 Trieste, TS, Italy
- ⁸⁴ INFN, Sezione di Trieste, Via Valerio 2, 34127 Trieste, TS, Italy
- ⁸⁵ Institut de Physique Théorique, CEA, CNRS, Université Paris-Saclay, 91191 Gif-sur-Yvette Cedex, France
- ⁸⁶ INFN-Bologna, Via Irnerio 46, 40126 Bologna, Italy
- ⁸⁷ Dipartimento di Fisica e Scienze della Terra, Università degli Studi di Ferrara, Via Giuseppe Saragat 1, 44122 Ferrara, Italy
- ⁸⁸ INAF, Istituto di Radioastronomia, Via Piero Gobetti 101, 40129 Bologna, Italy
- ⁸⁹ University of Lyon, UCB Lyon 1, CNRS/IN2P3, IUF, IP2I Lyon, France
- ⁹⁰ INAF-Istituto di Astrofisica e Planetologia Spaziali, Via del Fosso del Cavaliere, 100, 00100 Roma, Italy
- ⁹¹ INAF-IASF Bologna, Via Piero Gobetti 101, 40129 Bologna, Italy
- ⁹² School of Physics, HH Wills Physics Laboratory, University of Bristol, Tyndall Avenue, Bristol BS8 1TL, UK
- ⁹³ Instituto de Física Teórica UAM-CSIC, Campus de Cantoblanco, 28049 Madrid, Spain
- ⁹⁴ Research Program in Systems Oncology, Faculty of Medicine, University of Helsinki, Helsinki, Finland
- ⁹⁵ Department of Physics, PO Box 64, 00014 University of Helsinki, Finland
- ⁹⁶ Department of Physics, Lancaster University, Lancaster LA1 4YB, UK
- ⁹⁷ Department of Physics and Astronomy, University College London, Gower Street, London WC1E 6BT, UK
- ⁹⁸ Helsinki Institute of Physics, Gustaf Hällströmin katu 2, University of Helsinki, Helsinki, Finland
- ⁹⁹ Centre de Calcul de l’IN2P3, 21 avenue Pierre de Coubertin, 69627 Villeurbanne Cedex, France
- ¹⁰⁰ Dipartimento di Fisica “Aldo Pontremoli”, Università degli Studi di Milano, Via Celoria 16, 20133 Milano, Italy
- ¹⁰¹ INFN-Sezione di Milano, Via Celoria 16, 20133 Milano, Italy
- ¹⁰² Dipartimento di Fisica, Sapienza Università di Roma, Piazzale Aldo Moro 2, 00185 Roma, Italy
- ¹⁰³ Institut für Theoretische Physik, University of Heidelberg, Philosophenweg 16, 69120 Heidelberg, Germany
- ¹⁰⁴ Zentrum für Astronomie, Universität Heidelberg, Philosophenweg 12, 69120 Heidelberg, Germany
- ¹⁰⁵ INFN, Sezione di Lecce, Via per Arnesano, CP-193, 73100 Lecce, Italy
- ¹⁰⁶ Department of Mathematics and Physics E. De Giorgi, University of Salento, Via per Arnesano, CP-193, 73100 Lecce, Italy
- ¹⁰⁷ Institute for Computational Science, University of Zurich, Winterthurerstrasse 190, 8057 Zurich, Switzerland
- ¹⁰⁸ Departamento de Física, FCFM, Universidad de Chile, Blanco Encalada 2008, Santiago, Chile
- ¹⁰⁹ Department of Physics, PO Box 35 (YFL), 40014 University of Jyväskylä, Finland
- ¹¹⁰ Ruhr University Bochum, Faculty of Physics and Astronomy, Astronomical Institute (AIRUB), German Centre for Cosmological Lensing (GCCL), 44780 Bochum, Germany

Appendix A: Delivered data products

The new mosaics and associated products can be obtained from the IRSA website¹¹. The file naming convention for the stacks is as follows:

`CDS_{field}_ch{N}_{type}_v24.fits`,

where `field` is the field name, `N` is the channel number, and `type` is one of the following:

`ima`: flux image
`cov`: coverage in terms of number of frames used to build each pixel of the mosaic
`tim`: exposure time in seconds of the pixel
`unc`: uncertainty as determined from the standard deviation of the image pixels that contributed to the mosaic pixel

Table A.1 also gives the precise J2000 coordinates of the field tangent point in decimal degrees, the reference pixel corresponding to that tangent point, and the size, in pixels, of the mosaics. These values are the same for all channels of a field and for all the ancillary images. The pixel scale is 0'60 per pixel for all mosaics.

Table A.1. Data products information

Field	Longitude	Latitude	<i>x</i> -size	<i>y</i> -size	<i>x</i> -ref.pix	<i>y</i> -ref.pix
EDF-N	269.485804	66.590708	27 410	30 148	13 705.55	15 074.53
EDF-F	53.062008	-28.205431	23 751	26 204	11 876.02	13 102.29
EDF-S	61.301724	-48.496065	41 676	33 976	20 838.59	16 988.50
COSMOS	150.178292	2.220994	15 440	17 804	7 720.46	8 902.40
EGS	214.781187	52.720882	11 278	13 649	5 639.32	6 824.97
HDFN	189.405434	62.373754	11 813	1 979	5 907.03	8 489.78
XMM	34.101249	-4.598575	47 583	25 022	23 791.97	12 511.69

Notes. Longitude and latitude are equatorial and J2000, for the image tangent point. These values are valid for all four channels of each field and for their ancillary images.

The tables with the observation date, coordinates, position angles, and exposure times of the input frames are provided in IPAC format and are gzipped to reduce their size. Their names are as follows:

`CDS_{field}_ch{N}_info_v24.tbl.gz`.

The first few lines of the table for channel 1 of the EGS field are as follows:

	MJD	RA	DEC	PA	ExpTime
	double	double	double	double	double
	day	deg	deg	deg	sec
	null	null	null	null	null
53822.6296863	214.4583644468008	51.9912156620541	-126.246899270774		0.4
53822.6297117	214.4583644468008	51.9912156620541	-126.247055616923		10.4
53822.6298641	214.4583644468008	51.9912156620541	-126.246928305428		96.8
53822.6312156	214.383044470269	52.0556500561605	-126.304483006668		96.8

The coordinates are in degrees of longitude and latitude (Equatorial, J2000), and the PAs are measured eastward of north.

Appendix B: Coverage maps

Figures B.1 and B.2 show the full set of pixel exposure time maps for channels 1 and 3; channels, 2 and 4 are similar though slightly shifted in location. A square root scaling is applied in order to emphasise the differences at the low levels, and the same maximum is used for all fields in each channel. As EDF-S was not observed in channel 3, a blank field is placed there.

¹¹ https://irsa.ipac.caltech.edu/data/SPITZER/Cosmic_Dawn/

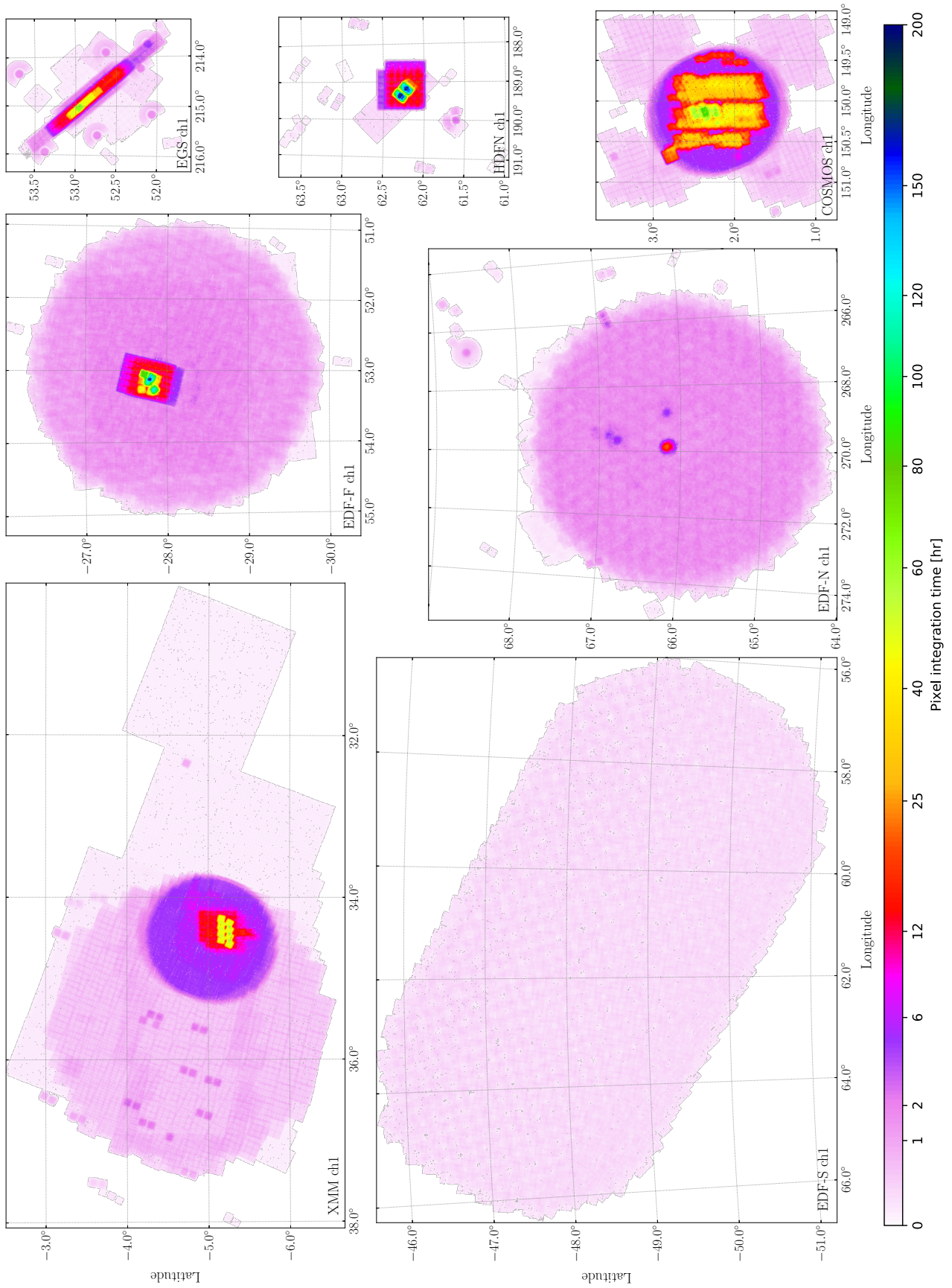


Fig. B.1. Integration time maps for channel 1.

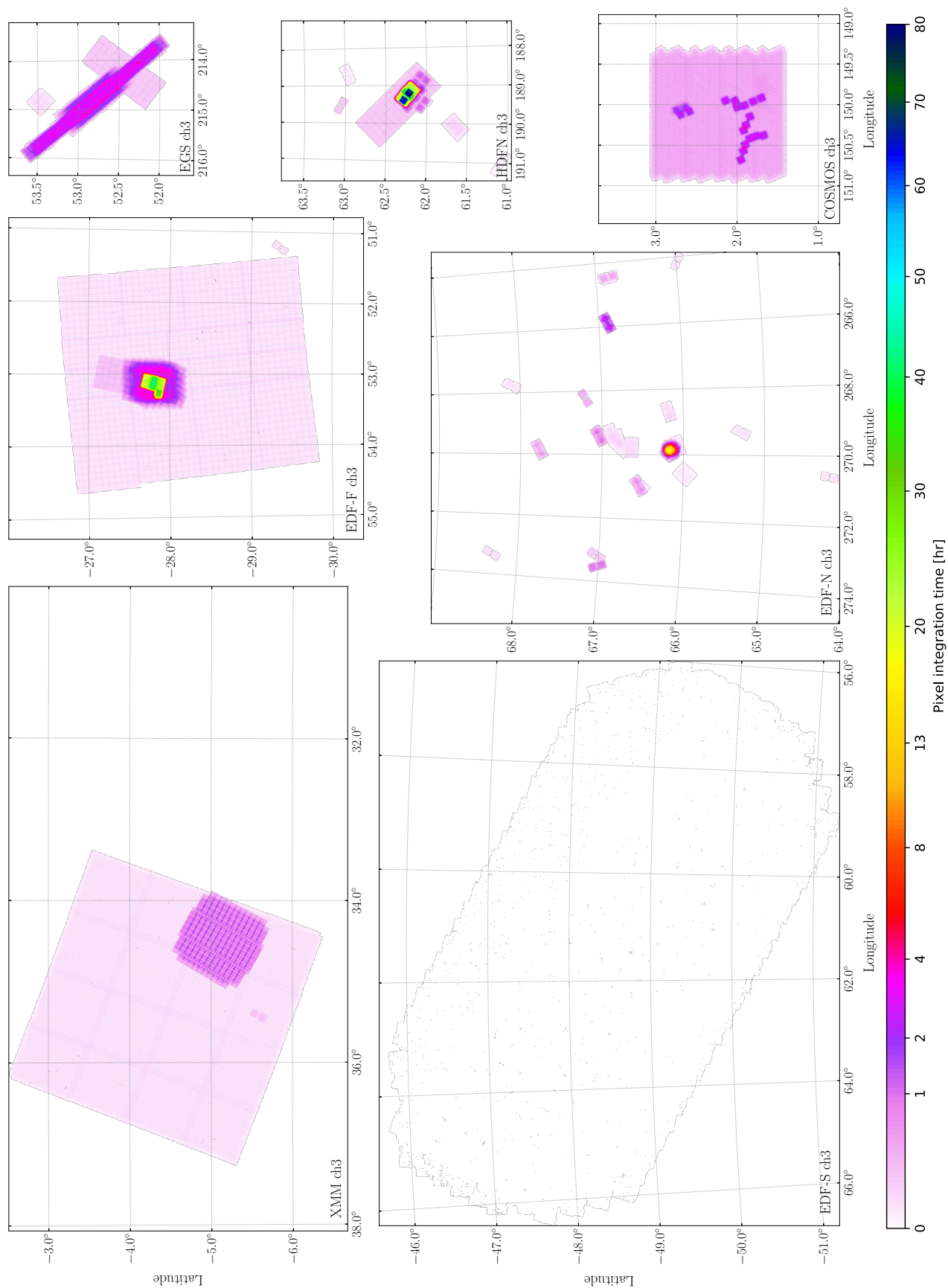


Fig. B.2. Integration time maps for channel 3. A blank field is included for EDF-S, which was not observed in that channel, and in order to have the same structure as B.1.

Appendix C: PID numbers

Table C.1 lists the *Spitzer* Space Telescope programme IDs (PIDs) of all the observations processed here. The ones of the observing programmes that we planned for this work are in bold, and the others are of the other archival observations that we reprocessed.

Table C.1. *Spitzer* Space Telescope Program IDs

Field	PIDs
EDF-N	68 609 613 618–624 1101 1125 1188 1189 1191–1200 1317 1334 1600–1700 1910–1949 1951 1953–1961 1963–1983 2314 3286 3329 3672 10147 11161 13153 20466 30432 40385 60046 70062 70162 80109 80113 80243 80245 90209
EDF-F	81 82 184 194 2313 11080 13058 20708 30866 40058 60022 61009 61052 70039 70145 70204 80217
EDF-S	14235
COSMOS	10159 11016 12103 13094 13104 14045 14081 14203 20070 40801 50310 61043 61060 70023 80057 80062 80134 80159 90042
EGS	8 10084 11065 11080 13118 20754 41023 60145 61042 80069 80156 80216 90180
HDFN	81 169 1304 10136 11004 11063 11080 11134 12095 13053 20218 30411 30476 40204 60122 60145 61040 61062 61063 70162 80215
XMM	181 3248 10042 11086 40021 60024 61041 61060 61061 70039 70062 80149 80156 80159 80218 90038 90175 90177